Solar Energy 198 (2020) 343–354

Contents lists available at ScienceDirect

Solar Energy

journal homepage: www.elsevier.com/locate/solener

Conjugate heat transfer model for feedback control and state estimation in a volumetric solar receiver

Benjamín Herrmann[a,b,*], Masoud Behzad[c], José M. Cardemil[d], Williams R. Calderón-Muñoz[d,e], Rubén M. Fernández[d]

[a] Department of Mechanical Engineering, University of Washington, 3900 E Stevens Way NE, Seattle, WA 98195, USA
[b] Institut für Strömungsmechanik, Technische Universität Braunschweig, Hermann-Blenk-Str. 37, 38108 Braunschweig, Germany
[c] Industrial Engineering School, Faculty of Engineering, Universidad de Valparaíso, Brasil 1786, Valparaíso, Chile
[d] Department of Mechanical Engineering, FCFM, Universidad de Chile, Beauchef 851, Santiago, Chile
[e] Energy Center, FCFM, Universidad de Chile, Av. Tupper 2007, Santiago, Chile

ARTICLE INFO

Keywords:
Volumetric solar receiver
Conjugate heat transfer
Reduced-order model
Feedback control
State estimation

ABSTRACT

Open volumetric solar receivers (VSRs) are a promising technology for concentrated solar power plants due to their capability to provide heat using ambient air as the working fluid operating at temperatures over 700 °C. Nevertheless, VSRs are challenged by the unsteadiness and high intensity of the radiation flux, which may cause unreliable or unsafe outflow temperatures, and may compromise the lifetime of the porous ceramic absorbers due to extreme thermal loads, thermal shock or thermal fatigue. We propose a data assimilation framework to address these matters using blower actuation, measurements from sensors located in the outflow stream of air, and a model for the conjugate heat transfer in an open VSR. We formulate said model and compare it against full three-dimensional CFD simulations to show that it captures the relevant dynamics while reducing the computational cost enough to allow for online calculations. A linear quadratic Gaussian (LQG) controller is used with the model to perform simultaneous state estimation and feedback control in three simulated scenarios. Our framework proves capable of stabilizing outflow air temperatures during the passing of a cloud, estimating the radiation flux hitting the absorber during daily operation, monitoring temperature cycling in the solid matrix, and avoiding extreme temperature gradients during start-up procedures. Artificial noise and disturbances are added to the system for all scenarios and the LQG controller proves to be robust, rejecting disturbances and attenuating noise, as well as compensating for model uncertainty.

1. Introduction

The growing awareness of the effect regarding the process of climate change has fostered the deployment of renewable energy sources for electricity generation. In that context, the most matures and economically viable renewable technologies are wind and photovoltaic (PV), which currently are cost competitive with conventional (fossil) power plants, showing a significant increment on the deployment of such plants during the last decade, moving from an installed capacity of 221 GW in 2010, to 941 GW in 2017 (REN21 Secretariat, 2012; REN21 Secretariat, 2018). Indeed, these two sources concentrates around 95% of the total investment in Renewable Energy, during 2017 (REN21 Secretariat, 2018). The power generation from wind and solar PV are characterized by high variations on their availability, due to environmental factors. However, the inherent variability of wind and PV power raises new challenges for power systems operators and regulators (Lott and Kim, 2014).

The Concentrating Solar Power (CSP) technologies stands out as one of the best options for delivering dispatchable electricity, and among the CSP plants Central Receiver Systems (CRS) have received larger attention during the last years, since it allows achieving higher operating temperatures, and therefore higher conversion efficiencies (IEA, 2010). Currently the most common application of CRS considers molten salts as working fluid and storage media, which limits its operating temperature to the chemical stability limit of the salt. In order to overcome such limit, the utilization of compressible gases as working fluid have been pointed out as a feasible option (Mehos et al., 2017). Indeed, several authors have proposed the use of super-critical carbon dioxide as working fluid in closed Brayton Cycles (Atif and Al-Sulaiman, 2017; Reyes-Belmonte et al., 2016). Nevertheless, using air

* Corresponding author at: Department of Mechanical Engineering, University of Washington, 3900 E Stevens Way NE, Seattle, WA 98195, USA.
E-mail address: benherrm@uw.edu (B. Herrmann).

https://doi.org/10.1016/j.solener.2020.01.062
Received 28 July 2019; Received in revised form 2 December 2019; Accepted 22 January 2020

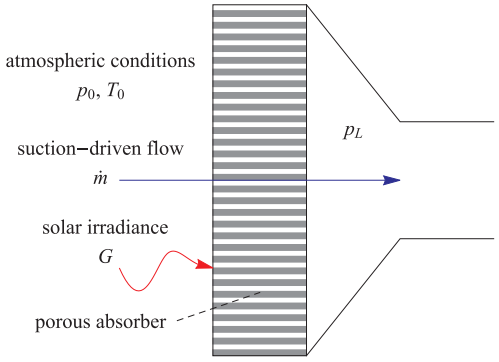

Fig. 1. Schematic representation of a volumetric solar receiver module.

as working fluid also presents several advantages, such as non toxicity, low cost, high availability, stability at high temperatures and low environmental impact (Ávila-Marín, 2011).

The use of air as working fluid in CRS requires a special design on the receiver that allows to efficiently convert the energy in solar radiation into useful heat. Several designs have been proposed during the last decades, but the best compromise between heat transfer and pressure drop is observed in the so-called open volumetric solar receiver (VSR) (Ávila-Marín, 2011). Typically, these receivers are comprised of hundreds of absorber modules, each of them with a cross-section on the order of 150 cm^2 (Ávila-Marín, 2011). A single VSR module consists of a permeable porous ceramic that allows concentrated solar radiation to penetrate within its structure, thus enhancing convective heat exchange with a suction-driven flow of atmospheric air, as shown in Fig. 1.

The operation of CRS requires the availability of smart control systems, that allows dealing with the fast transient events, which induce significant stress in the receiver (Augsburger and Favrat, 2013). The solar receiver is one of the critical components in CRS, representing a significant share of the capital investment (Gielen, 2012). Therefore, cloud passing over the heliostat field strongly affects the operation of the system. Transient variations on the incident radiation flux distribution increase the thermal stresses in the receiver, leading to severe damages or to reduce the cyclic life of the device (Crespi et al., 2018). Since the transient variation on the solar beam radiation are unavoidable, several authors have proposed different approaches for handling that issue, such as manipulate the heliostats aiming to the receiver (García et al., 2018; Tehrani and Taylor, 2016), or controlling the working fluid flow rate, which is particularly interesting for open volumetric receiver systems (Li et al., 2016).

Hence, the availability of accurate estimation models for predicting the state and the actual operating temperature of the solid matrix in the volumetric absorber, would allow a safe and efficient operation of the plant. Indeed, such estimation models would also allow feedback control of the fluid outlet temperature, which is crucial for avoiding dysfunctions with the processes downstream: electricity generation, industrial process, etc. In addition to that, an appropriate monitoring of the receiver temperature cycling also allows to estimate the remaining life of the components and preventing dramatic failures (Li et al., 2016). Several works have pointed out that the solar flux distribution on the receiver surface or inside the absorber is highly non-uniform (Ávila-Marín, 2011; Augsburger and Favrat, 2013; Tehrani and Taylor, 2016), therefore it is crucial to determine the actual incident radiation flux for a safe operation. However, since measuring that flux is highly complex, developing models capable of online estimation seems as an efficient approach.

Previous studies have proposed estimation models for saturated steam and molten salts receivers. Augsburger and Favrat (2013) developed a simulation model for evaluating the cloud passages on a heliostat field, but considering an analytic function (based on the convolution of different Gaussian distributions) for estimating the radiation flux distribution on the receiver. The results of the model allowed to assess the flux evolution over short periods in terms of the geometrical spread on the receiver surface, the flux peaks and gradients, among other parameters. Later, Samanes and Garcia-Barberena (2014) developed a transient cavity receiver model, in which the main heat transfer mechanisms were modeled in fast approach, allowing to analyze the impact of introducing an adaptive control able to predict the dynamic response of the receiver for different operating conditions.

Recently, Li et al. (2016) modeled an open-loop air receiver, coupled to a thermal energy storage. The model was validated against experimental data, allowing to adjust the heat transfer equations by using appropriate Nusselt correlations. In that context different control strategies were analyzed, aiming to keep the receiver outlet air temperature stable and control the integration to the thermal energy storage. However, that model was not applied to capture the impact of fast transient events such as cloud passing, which demands much more complex control schemes. Finally, Crespi et al. (2018) presented an analysis of the performance of a central receiver plant using molten salts as working fluid. The authors analyzed the dynamic behavior of the receiver when subjected to transient conditions due to the passage of clouds, considering different scenarios and assessing the receiver response. However, the control measures were applied to the heliostat field aiming control and not to the fluid system, as expected for systems with larger thermal inertia.

In this study, we propose the implementation of a physics based approach, which accounts for the conjugate heat transfer phenomena in a volumetric receiver module, and implement a linear quadratic Gaussian (LQG) controller. Feedback control would not only allow the stabilization of the temperature outlet of the receiver (even under fast transient conditions), but also the estimation of the flux distribution. The subsequent sections of this article are organized as follows. Section 2 describes the analytical formulation of the proposed model, and a brief review on the tools borrowed from optimal control theory is presented for completeness. Section 3 presents the methodology for implementing the model and the control scheme proposed, which is later evaluated in terms of the results of Section 4. The results are presented under different scenarios of transient behavior, allowing to capture the impact and the advantages of the new approach. Finally, Section 5 concludes and highlights the future challenges for the proposed framework.

2. Analytic framework

2.1. Model formulation

The purpose of this section is to derive a physics-based reduced-order model for the dynamics of the heat transfer processes in an open VSR module. In particular, we are interested in describing the behavior of the outlet temperature for the fluid, and of the temperature and temperature uniformity for the solid matrix of the porous absorber. Following the principle of Ockham's razor, we propose a minimal representation of the system using only three degrees of freedom. Let T_r represent the temperature of the solid matrix at the frontal section of the receiver, where the incoming radiation flux hits and penetrates into the absorber up to a depth L_r. Let then T_c be the bulk temperature of the solid matrix in the rear section of the receiver of length L_c, which gets heated through conduction with the frontal section. The fluid enters the receiver of length $L = L_r + L_c$ at a temperature T_0, it exchanges heat with both sections of the solid matrix by means of convection and its temperature quickly saturates to the outlet value, which we will call T_a. These heat transfer processes are shown in Fig. 2, as well as the typical streamwise temperature distributions of the fluid and of the solid matrix.

We start by tackling the hydrodynamics governing the problem. A blower produces a suction pressure p_L at the receiver outlet which is

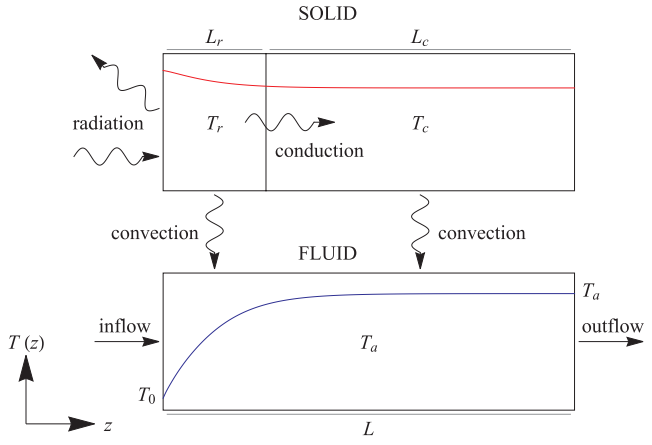

Fig. 2. Schematic of the heat transfer processes in a volumetric solar receiver and the reduced-order model. The blue (red) curve shows a typical streamwise temperature distribution of the fluid (solid matrix). (For interpretation of the references to colour in this figure legend, the reader is referred to the web version of this article.)

lower than the atmospheric pressure p_0, and therefore induces a flow of air through the porous structure. Due to conservation of mass, the mass flow density $\dot{m}$ is constant through the receiver. The momentum balance determines the relation of $\dot{m}$ with the pressure difference between both sides of the porous structure. In a similar manner to that presented in the work of Becker et al. (2006), we obtain this relation using Darcy-Forcheimer's law and the ideal gas equation of state, as follows

$$\frac{p_0^2 - p_L^2}{2RT_aL} = K_1\mu\dot{m} + K_2\dot{m}^2, \tag{1}$$

where $\dot{m}$ is expressed per unit area of receiver, R is the ideal gas constant for air, K_1 and K_2 are the linear and quadratic hydraulic resistance coefficients respectively, and μ is the dynamic viscosity of air. In Eq. (1) the hydrodynamic transients have been neglected because the residence time of the fluid inside the absorber is much shorter than the time scales associated with the thermal response.

Due to the large changes in the air temperature as it flows through the absorber, it is important to take into account the variations of viscosity. As in Kribus et al. (1996), the temperature dependency is approximated using a power-law of the form $\mu_0(T/T_0)^{n_\mu}$, where μ_0 is the viscosity at ambient temperature and $n_\mu = 0.7$. This power-law is evaluated at the average of fluid and solid matrix temperatures at the frontal and rear sections of the receiver. Then an effective viscosity is calculated using an average between sections weighted by their depth, as follows

$$\mu = \frac{\mu_0}{L}\left(L_r\left(\frac{T_r + T_{a0}}{2T_0}\right)^{n_\mu} + L_c\left(\frac{T_c + T_a}{2T_0}\right)^{n_\mu}\right), \tag{2}$$

where T_{a0} is the mean fluid temperature at the frontal section of the receiver. We assume a quadratic temperature profile varying from T_0 to T_a and having zero derivative at $z = L_r$, thus integrating we get a mean value of $T_{a0} = T_0 + 2/3(T_a - T_0)$. This approximation is inspired by the typical variations of the fluid temperature through the absorber, as shown by the blue curve in Fig. 2.

Substituting μ from Eq. (2) into Eq. (1), and given a value for the suction pressure p_L, the mass flow density $\dot{m}$ can be solved for as a nonlinear function of the system state $(T_a, T_r, T_c)^T$. Thus, the dynamics of the system is governed by the thermal energy balances for the fluid and the two solid sections

$$M_ac_a\frac{dT_a}{dt} = -\dot{m}c_a(T_a - T_0) + h_{ra}A_{ra}(T_r - T_{a0}) + h_{ca}A_{ca}(T_c - T_a), \tag{3a}$$

$$M_rc_r\frac{dT_r}{dt} = -h_{ra}A_{ra}(T_r - T_{a0}) - h_{rc}A_{rc}(T_r - T_c) + \varepsilon G - \varepsilon\sigma(T_r^4 - T_0^4), \tag{3b}$$

$$M_cc_c\frac{dT_c}{dt} = -h_{ca}A_{ca}(T_c - T_a) + h_{rc}A_{rc}(T_r - T_c), \tag{3c}$$

where M_a and c_a are the mass of fluid inside the receiver and its heat capacity, M_r, c_r, M_c and c_c are the masses and heat capacities of the solid matrix frontal and rear sections respectively, h_{ra} and h_{ca} are the convective coefficients for the heat transfer through the surfaces A_{ra} and A_{ca} between the fluid and the corresponding section of the solid matrix, $h_{rc} = 2k_{rc}/L$ is the thermal conductance for the heat transfer through the surface A_{rc} between solid matrix sections where the material has a thermal conductivity k_{rc}, G is the direct radiation flux delivered by the heliostat field, ε is the absorber emissivity, σ is the Stefan–Boltzmann constant, and t is time. The solid matrix is assumed to behave as a grey body under radiative equilibrium, therefore its emissivity is equal to its absorptivity (Modest, 2013). All masses and surface areas in Eqs. (3) are expressed per unit area of receiver cross-section.

Temperature dependency of the thermal conductivity of air is important for the range of conditions studied, hence its effect on the heat transfer coefficients is also approximated with a power-law and evaluated at the respective film temperatures, as follows

$$h_{ra} = h_0\left(\frac{T_r + T_{a0}}{2T_0}\right)^{n_h}, \quad h_{ca} = h_0\left(\frac{T_c + T_a}{2T_0}\right)^{n_h}, \tag{4}$$

where $n_h = 0.88$ and h_0 is the heat transfer coefficient calculated using the thermal conductivity of air evaluated at T_0. This value of n_h was obtained by a least-squares fit of a power-law to the data set for the thermal conductivity of air as a function of temperature in the range 300–1400 K presented in the book by Cengel and Ghajar (2011). Note that T_{a0} is used for the convective heat exchange and all fluid properties at the front section of the receiver, as it better approximates the fluid temperature at this streamwise location.

2.2. Linear quadratic Gaussian control

This section presents a brief outline of the linear quadratic Gaussian (LQG) framework used with the reduced-order model. Eqs. (3) represent a nonlinear dynamical system and can be rewritten as $\dot{\mathbf{x}} = \mathbf{f}(\mathbf{x}, \mathbf{u})$, where $\mathbf{x} = (T_a, T_r, T_c)^T$ is the state vector, the overdot denotes time differentiation, and $\mathbf{u}$ is a control input, such as p_L for blower actuation. A linear state-space model is obtained by linearizing around an equilibrium point, as follows

$$\dot{\mathbf{x}} = \mathbf{A}\mathbf{x} + \mathbf{B}\mathbf{u}, \tag{a}$$

$$\mathbf{y} = \mathbf{C}\mathbf{x}, \tag{b}$$

where the matrices $\mathbf{A}$ and $\mathbf{B}$ arise from the linearization, $\mathbf{x}$ and $\mathbf{u}$ now represent the deviation from the state and actuation equilibrium points respectively, and $\mathbf{y}$ represents linear measurements of the system state given by the mapping $\mathbf{C}$. For an arbitrary control signal $\mathbf{u}(t)$, the exact solution to Eq. (a) becomes

$$\mathbf{x}(t) = e^{\mathbf{A}t}\mathbf{x}(0) + \int_0^t e^{\mathbf{A}(t-\tau)}\mathbf{B}\mathbf{u}(\tau)d\tau. \tag{6}$$

As described by Eq. (6), the temporal evolution of the state is governed by the matrix exponential and the convolution integral. The system given by Eqs. (5) is said to be *controllable*, if it is possible to navigate from the origin to an arbitrary state $\mathbf{x}$ within finite time using a finite control signal $\mathbf{u}(t)$, see, e.g., Aström and Murray (2010). In addition, if measurements of the full state are available, then $\mathbf{C} = \mathbf{I}$ is the $N_x \times N_x$ identity matrix, where N_x is the dimension of $\mathbf{x}$. In this case, it is possible to design a proportional controller $\mathbf{u} = -\mathbf{K}_r\mathbf{x}$ to arbitrarily place the eigenvalues of the closed-loop system

$$\dot{\mathbf{x}} = \mathbf{A}\mathbf{x} + \mathbf{B}\mathbf{u} = (\mathbf{A} - \mathbf{K}_r)\mathbf{x}. \tag{7}$$

A typical control goal is to stabilize the system by trading off between how fast we drive the state $\mathbf{x}$ to $\mathbf{0}$ and how expensive the control actuation is. For this purpose, the controller gain $\mathbf{K}_r$ is constructed so that it minimizes a quadratic cost function J_r that balances the aggressive regulation of $\mathbf{x}$ with the control expenditure, as follows

$$J_r = \int_0^\infty (\mathbf{x}^T(\tau)\mathbf{Q}\mathbf{x}(\tau) + \mathbf{u}^T(\tau)\mathbf{R}\mathbf{u}(\tau))\mathrm{d}\tau, \tag{8}$$

where the matrix $\mathbf{Q}$ is positive semi-definite and the matrix $\mathbf{R}$ is positive definite. The entries in $\mathbf{Q}$ and $\mathbf{R}$ weight the cost of deviations of the state from zero and the cost of actuation, respectively. The full-state feedback controller $\mathbf{K_r}$ that minimizes the quadratic cost function J_r is called a linear quadratic regulator (LQR), and can be calculated by numerically solving an algebraic Riccati equation using built-in routines from many computational packages.

The optimal LQR controller described above relies on access to full-state measurements of the system, which is hardly the case in practical applications. In the context of this work, $\mathbf{y}$ is usually given by outflow temperature readings T_a, as sensors in the solid matrix are often unavailable. The system given by Eqs. (5) is said to be *observable* if any state $\mathbf{x}$ can be estimated from the time-history of sensor measurements $\mathbf{y}$, see, e.g., Aström and Murray (2010). A full-state estimator is a dynamical system that produces an estimate $\hat{\mathbf{x}}$ of the full state $\mathbf{x}$, given our knowledge of the process dynamics, the control input $\mathbf{u}$, and the sensor measurements $\mathbf{y}$. If the system is *observable*, a full-state estimator can be constructed using a filter gain $\mathbf{K}_f$, as follows

$$\dot{\hat{\mathbf{x}}} = \mathbf{A}\hat{\mathbf{x}} + \mathbf{B}\mathbf{u} + \mathbf{K}_f(\mathbf{y} - \hat{\mathbf{y}}), \tag{9a}$$

$$\hat{\mathbf{y}} = \mathbf{C}\hat{\mathbf{x}}, \tag{9b}$$

A typical estimator goal is for the estimated state $\hat{\mathbf{x}}$ to converge quickly to the true state $\mathbf{x}$, while considering how much the model is trusted, which may have disturbances and missing dynamics, and how much the sensor measurements are trusted, which may have noise. Analogously to the LQR procedure, the estimator gain $\mathbf{K}_f$ is constructed so that it minimizes a quadratic cost function J_f that balances aggressive estimation with noise attenuation, as follows

$$J_f = \lim_{t\to\infty} \mathbb{E}((\mathbf{x}(t) - \hat{\mathbf{x}}(t))^T(\mathbf{x}(t) - \hat{\mathbf{x}}(t))), \tag{10}$$

where $\mathbb{E}$ is the expected value operator. The real system has state disturbances $\mathbf{d}$ and sensor noise $\mathbf{n}$, which are assumed to be zero-mean Gaussian white-noise processes with known covariances $\mathbf{V}_d$ and $\mathbf{V}_n$, respectively. These covariances appear implicitly in the calculation of the cost function J_f. The entries in the matrices $\mathbf{V}_d$ and $\mathbf{V}_n$ weight the uncertainty level of the model and that of the sensor measurements, respectively. The full-state estimator $\mathbf{K_f}$ that minimizes the quadratic cost function J_f is called a linear quadratic estimator (LQE) or Kalman filter, and, as for the LQR, can be calculated by numerically solving another algebraic Riccati equation using built-in routines from many computational packages.

A linear quadratic Gaussian (LQG) controller is the optimal sensor-based feedback control law that minimizes the cost function in Eq. (8) including sensor noise and state disturbances. Remarkably, the optimal LQG solution can be obtained by combining the LQR controller gain $\mathbf{K}_r$ with the estimated state $\hat{\mathbf{x}}$ obtained by the Kalman filter gain $\mathbf{K}_f$, where $\mathbf{K}_r$ and $\mathbf{K}_f$ are each optimal in their corresponding cost functions. Thus, it is possible to calculate $\mathbf{K}_r$ and $\mathbf{K}_f$ separately and then combine them to form an optimal LQG controller, as shown in Fig. 3.

For more details on linear systems and optimal control theory, the readers are referred to textbooks such as Aström and Murray (2010, 1994, 2013).

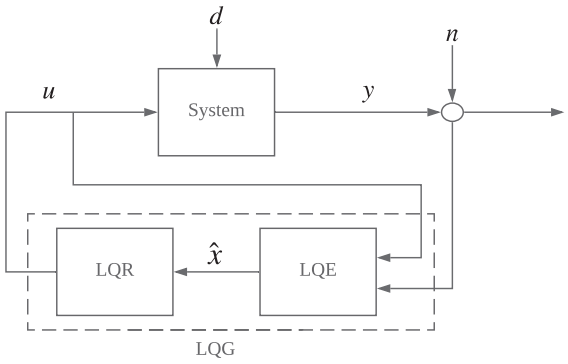

Fig. 3. Block diagram for a linear quadratic Gaussian (LQG) controller.

3. Methodology

3.1. Model parameters

Parameters appearing in the equations presented in Section 2.1 are selected to model a silicon carbide honeycomb absorber of prorosity $\phi = 0.64$ and square channels of height $l = 2$ mm. The cross-sectional area of the solid matrix per unit area of receiver cross-section is calculated as $A_{rc} = (1 - \phi)$. The areas for the convective heat exchange at the front and rear parts of the receiver are also normalized by the cross-sectional area of the absorber, and are therefore calculated as $A_{ra} = 4L_r\phi/l$ and $A_{ca} = 4L_c\phi/l$, respectively, where L_r and L_c are the corresponding streamwise lengths. The parameter values that remain constant throughout this study are listed in Table 1.

The length of the frontal receiver section L_r is based on the penetration depth of radiation flux into the absorber, which is calculated from the view factor expression for a honeycomb monolith presented in Worth et al. (1996). The linear and quadratic hydraulic resistance coefficients K_1 and K_2 are calculated using standard correlations for the friction factor for fully developed and developing laminar flow in a square duct, respectively. The convective heat transfer coefficient h_0 is calculated from the Nusselt number for thermally developed square duct flow at constant wall temperature, also using standard correlations, such as those presented in, e.g., Kandlikar et al. (2005).

3.2. CFD simulations

In addition to simulations using the model presented above, full three-dimensional computational fluid dynamics (CFD) simulations using ANSYS CFX are also carried out for comparison purposes. Using CFD for analyzing the performance of volumetric receivers have been considered by several authors Abuseada et al. (2019,), showing good agreement with experimental data. The model implemented herein follows the recommendations from the literature and considers the mass, momentum and energy balances within the porous absorber module of a VSR. Details of the solver setting and the numerical methodology are described below.

The porous media is treated as a continuum, hence there is only one computational domain which is shared between fluid and solid phases, as presented in the work by Fend et al. (2013,). The governing equations are continuity, unsteady and compressible Navier–Stokes with an ideal gas law, and unsteady energy balances under the non-thermal equilibrium assumption between fluid and solid phases. The continuum approach considers a volume-average of physical quantities at the pore level, therefore porosity of the absorber, $\phi = 0.64$, and interactions at the fluid–solid interface enter the governing equations as source terms (Kaviany, 2012).

The computational domain consists of a single absorber module with a square cross-section of 100 mm × 100 mm and a depth $L = 40$ mm. Hydrodynamic boundary conditions are a no-slip condition

Table 1
Constant parameters for the reduced-order model.

L	L_r	L_c	T_0	K_1	K_2	μ_0	h_0	k_{rc}	
40 mm	10 mm	30 mm	25 °C	1.1×10^7 m^{-1}	46.68 m^{-2}	18.3 μPa	38.89 W/m^{2}K	80 W/m K	
l	ϕ	M_r	M_c	c_a	c_r	c_c	A_{ra}	A_{ca}	A_{rc}
2 mm	0.64	11.52 kg/m^2	34.56kg/m^2	1008 J/kgK	750 J/kgK	750 J/kgK	12.8	38.4	0.36

at the side-walls, zero (relative) total pressure at the inlet surface, and a prescribed suction pressure at the outlet p_L. The particular value used for p_L depends on the scenario being simulated and will be indicated accordingly. An adiabatic boundary condition is used for the fluid and the solid at the side-walls and outlet surfaces. At the front surface (flow inlet), a fixed temperature of $T_{a0} = 25$ °C is set for the air, and for the solid fraction, a temperature-dependent heat flux $q_s(T_s)$ is used, as follows

$$q_s(T_s) = \varepsilon(1-\phi)(G - \sigma(T_s^4 - T_0^4)), \tag{11}$$

where T_s corresponds to the local value of the temperature in the solid phase. Eq. (11) corresponds to the surface balance between emission and the direct radiation flux hitting the front of the solid matrix. The value for G used depends on the scenario being simulated and is indicated accordingly. A similar radiative balance is considered at the interior of the computational domain using a volumetric heat source term $q_v(T, z)$ in the energy equation for the solid phase, as follows

$$q_v(T_s, z) = \frac{4\varepsilon\phi}{l} F(z)(G - \sigma(T_s^4 - T_0^4)), \tag{12}$$

where z is the streamwise coordinate, l is the channel height as presented in Table 1, and $F(z)$ is the view factor expression for a honeycomb monolith presented in Ref. (Worth et al., 1996). Eq. (12) represents the radiative balance between the internal walls of the absorber, the heliostats and the outside air. In the same manner as for our proposed model, in Eqs. (11) and (12) we consider that the receiver material behaves as a grey body under radiative equilibrium, therefore its emissivity and absorptivity are equal (Modest, 2013)

Other interactions at the pore level that are modeled as source terms in the continuum approach are the Darcy-Forcheimer momentum losses and the convective heat exchange between fluid and solid phases. In the same way as for the reduced-order model, the respective linear and quadratic loss coefficients, and the convective heat transfer coefficient are computed using standard correlations for friction factors and Nusselt number in square duct laminar flow (Kandlikar et al., 2005). A streamwise coefficient multiplier of 100 is used for the transverse directional loss coefficients to model the anisotropy of the hydraulic losses through a honeycomb absorber, as opposed to those in an open-cell foam absorber. The viscosity and thermal conductivity of air have a power-law temperature dependency, as presented in the model formulation section, with the difference that the properties are now evaluated at the local temperature average between fluid and solid phases. All other geometrical parameters or fixed thermophysical properties are the same as those presented in Table 1.

The domain is discretized using hexahedral elements generated by a sweep method, resulting in a mesh with quality metrics within the recommended values (Ansys Inc., 2012). Steady-state simulations are carried out for $G = 0.7$ MW/m^2 and $p_L = -65.04$ Pa (relative pressure) using different grids and increasing the number of elements until mesh independence is achieved. Finally, a mesh with 1.62×10^5 control volumes is selected. A high resolution advection scheme is selected, which includes a variable blend factor for the purpose of accuracy and robustness of the solution (Ansys Inc., 2011). It is also important to set a proper convergence criterion for the solver. The local imbalance can be evaluated by the root mean square (RMS) type of residual, while the global imbalance is checked by the conservation target, these are required to be below 10^{-5} and 10^{-3}, respectively. The simulation times for the different transient scenarios range between 14 and 31 h on a 4-core Intel® Xeon® E3-1240 v5 processor and 16 GB of RAM.

4. Results and discussion

4.1. Comparison with CFD: three scenarios

The purpose of this section is to compare steady and transient solutions obtained with the model to those obtained using full three-dimensional CFD. Moreover, the comparison of transient results is carried out for three simulated scenarios that are designed to emphasize the need for control and estimation. To solve for Eq. (2), we first obtain the expression of the positive root of Eq. (1) for the mass flow density $\dot{m}$ as a function of the temperatures and suction pressure with μ substituted in from Eq. (2). Subsequently, steady and transient solutions for Eq. (2) are computed in *Matlab* using a nonlinear equations solver based on the Trust-Region-Dogleg algorithm (Conn et al., 2000), and a variable-step and variable-order stiff differential equations solver (Shampine and Reichelt, 1997) respectively.

To start, we compute the steady solutions using a suction pressure p_L such that the air outflow temperature is $T_a = 700$ °C for different radiation fluxes ranging from $G = 0.4$–1.0 MW/m^2 with increments of 0.1 MW/m^2. For the CFD simulations, this is achieved using an outlet pressure boundary condition and iterating the value of p_L until the solution for the mass flow averaged outlet temperature reaches 700 ± 1 °C for each value of G. The solid matrix temperature in the front section of the receiver T_r is approximated from CFD results as the area average of the solid-phase temperature in the inlet surface of the computational domain. The solid matrix temperature in the rear section of the receiver T_c is calculated as the volume average of the solid-phase temperature in the whole computational domain. For the model results, a nonlinear equations solver from *Matlab* is used to find p_L, T_r and T_c such that the steady solution to Eqs. (3) satisfies $T_a = 700$ °C, for every value of G. Afterwards, the mass flow rate per unit area of absorber $\dot{m}$ is calculated from Eq. (1).

Steady state solutions for the mass flow rate and temperatures in the simulated VSR are shown in Fig. 4 for different radiation fluxes, where a satisfactory agreement is observed between model and CFD calculations. As the value of G increases, a higher mass flow rate is required to maintain the desired air outflow temperature, and larger temperature differences occur within the solid matrix.

4.1.1. Clear-sky daily operation

During clear-sky operation radiation flux incident on the receiver changes slowly throughout the day due to the variation on the incident solar radiation and because of different losses, such as cosine losses, alignment problems, astigmatism, shading and obstruction among others. In order to assess the operation under representative conditions, a simple analysis using a ray-tracing software was implemented. A cosine approximation was identified to be representative for describing that daily variations. During the operation of the system under such conditions, the mass flow going through the absorber has to be adjusted in order to maintain the desired outflow air temperature. To achieve this, the blower needs to be controlled to modify the suction pressure that induces the flow of air. Thus, the simulations of the daily operation

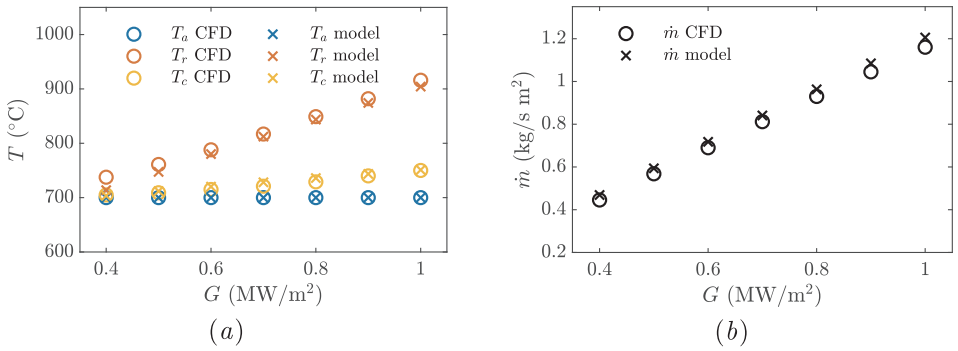

Fig. 4. Model and CFD steady state solutions for different values of the radiation flux. (*a*) Air outflow temperature and solid matrix temperatures in the front and rear sections of the receiver. (*b*) Mass flow rate per unit area of absorber.

during a clear-sky scenario are carried out using a constant mass flow rate to emphasize the need for control. As previously mentioned, the simulated scenario considers a time-dependent radiation flux that is periodic over an 8 h window, as follows

$$G(t) = G_{av} - G_A \cos(\omega t), \tag{13}$$

where $G_{av} = 0.7$ MW/m^2 is the daily average, $G_A = 0.3$ MW/m^2 is the amplitude of the variations and $\omega = 2\pi/(8 \times 3600)$ s^{-1} their angular frequency. The imposed radiation flux as function of time is shown in Fig. 5*a*). The outlet boundary condition for the CFD simulation is set to a fixed mass flow rate $\dot{m} = 0.812$ kg/sm^2 (per unit area of absorber), selected such that a radiation flux of G_{av} results in a desired steady state outflow air temperature of $T_a = 700$ °C. The daily behavior of air outflow temperature and solid matrix temperatures from the front and rear sections of the receiver are presented with a good agreement between model and CFD in Fig. 5*b*).

Without blower actuation to control the mass flow rate during daily operation, air outflow and solid matrix temperatures manifest variations of about ~500 °C, as shown in Fig. 5*b*). The need for control is evident, even if the solid matrix admitted such fluctuations (and peak values), changes of this magnitude on the air temperature are certainly not suitable for the downstream processes.

4.1.2. Cloud passing

The passing of a cloud may induce abrupt changes in the radiation flux hitting a VSR, causing large temperature variations in the solid matrix and working fluid. This scenario is simulated using a time-dependent radiation flux that starts at a value of 1 MW/m^2 and after 5s drops linearly over the next 5s to 0 MW/m^2, where it stays for 30s before increasing linearly over 5s back the starting value, as shown in Fig. 6*a*).The proposed scenario represents the worst case for a small heliostat field as featured by the currently operational CSP air systems. The approach considered herein is based on the analysis developed by Cagnoli et al. (2017) and García et al. (2018). A fixed suction pressure such that $T_a = 700$ °C when $G = 1$ MW/m^2 is used for computations with both, model and CFD (as outlet boundary condition in the latter). The fast temperature transients that occur in a VSR during a cloud passing are plotted in Fig. 6*b*).

A sharp drop of about ~700 °C in the air outflow and solid matrix temperatures is observed when the blower is not being actuated to adjust the mass flow rate, as shown in Fig. 6*b*). Control is clearly a necessity for reliability of the downstream processes, moreover, estimation of the temperatures in the solid matrix is required to monitor thermal expansion cycles that may occur several times per day.

4.1.3. Cold start-up

The cold start-up procedure carried out every day in a CSP plant involves gradually aiming the heliostats at the receiver and adjusting the mass flow of working fluid to take the system from rest to its operating condition. In a VSR, excessive temperature differences may occur within the absorber as it heats up, leading to thermal shock. Therefore, the control of the heliostat field and blower must balance the structural integrity of the VSR with a faster start-up of the plant. The cold start-up scenario is simulated with the model and CFD using a time-dependent radiation flux and suction pressure. At $t = 0$, the system is at rest with all temperatures set to $T_0 = 25$ °C, no heliostats aiming at the receiver, $G = 0$, and zero pressure drop $p_L = p_0$ so there is no flow of air. After 5s, the pressure drop and radiation flux ramp-up for 60 s to reach $G = 0.4$ MW/m^2 and the value of p_L that results in $T_a = 700$ °C in steady state. This time-dependency, shown in Fig. 7*a*) for the radiation flux, is selected to simulate a typical open-loop control strategy used for cold-start-up procedure and emphasize the utility of a more sophisticated approach.

Fig. 7*b*) shows the evolution of air outflow and solid matrix temperatures during a cold start-up procedure, while Fig. 7*c*) shows the evolution of temperature differences within the absorber. The linear ramp-up control strategy for the radiation flux and pressure drop results in a slow thermal response, taking about 600s to reach the steady

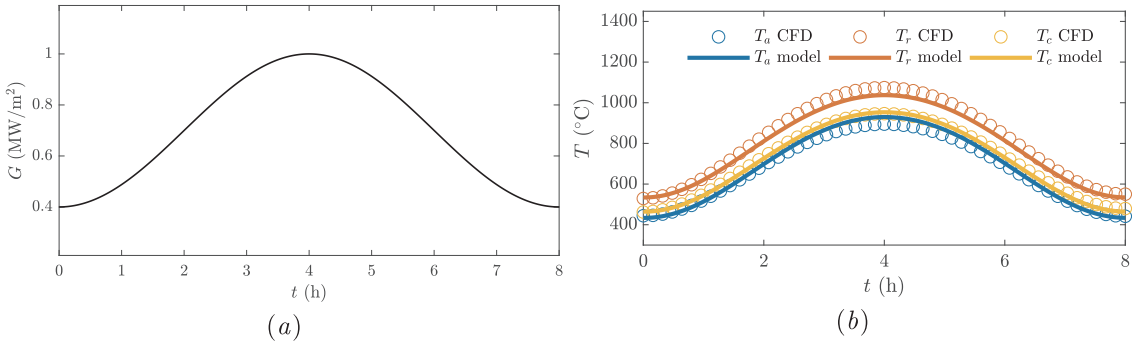

Fig. 5. (*a*) Time-dependent radiation flux used for the clear-sky daily operation scenario. (*b*) CFD and model results for air outflow temperature and solid matrix temperatures in the front and rear sections of the receiver during clear-sky daily operation.

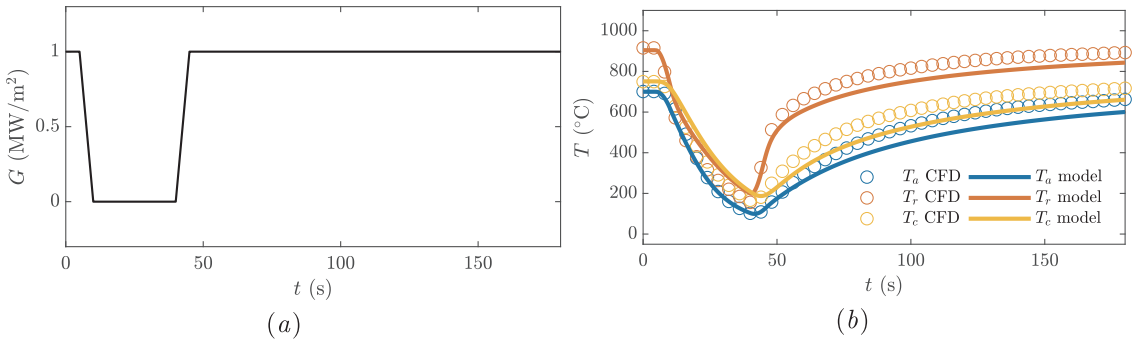

Fig. 6. (*a*) Time-dependent radiation flux used for the cloud passing scenario. (*b*) CFD and model results for air outflow temperature and solid matrix temperatures in the front and rear sections of the receiver during the passing of a cloud.

operation condition, and an overshoot more than 70 °C greater than the equilibrium value for the temperature differences within the absorber. In the same way as for the previous scenarios, the characteristic dynamics of the system are captured by the model.

4.2. Clear-sky daily operation with LQG

The formulation of the control problem involves the extension of the system to consider the pressure drop induced by the blower, $\Delta p = p_0 - p_L$, and the radiation flux reflected off the heliostat field, G, as new state variables. The following differential equations are included to describe the evolution of these variables

$$\dot{\Delta p} = u, \tag{14}$$

$$\dot{G} = 0, \tag{15}$$

where u is the only control input and represents the rate of change of the blower rotation rate. Even though radiation flux is changing, these variations are very slow when compared to the thermal response times of the system, hence Eq. (15) is a reasonable model. Furthermore, this allows for the inclusion of G as a state variable, which enables its estimation in real-time using sensor-based feedback from pressure drop and air outflow temperature measurements. The nonlinear system described by Eqs. (3) is simulated during clear-sky daily operation with the radiation flux shown in Fig. 5*a*) using LQG control based on the linearized system, which is extended to include Eqs. (14) and (15). For this scenario, the system is linearized around the equilibrium point $T_a = 700$ °C, $T_r = 713.7$ °C, $T_c = 703.5$ °C, $\Delta p = 24.76$ Pa, $G = 0.4$ MW/m^2, and $u = 0$ Pa/s.

Results for the simulation with LQG control are shown in Fig. 8, where the dashed curves correspond to the estimates of the state variables and the solid curves correspond to the actual behavior of the state variables of the nonlinear system. The controller stabilizes the air outflow temperature without using any measurements of the radiation flux. Furthermore, as shown in Fig. 8*c*), the estimated radiation flux is in agreement with the true value, thus enabling real-time evaluation of the receiver efficiency and diagnostics about its state of health.

In order to assess the robustness of the LQG controller, zero-mean Gaussian noise and disturbances with specified standard deviations are included in the simulations. Measurement noise with a standard deviation of 20 °C and 4 Pa is added directly to the air outflow temperature and pressure sensor readings, respectively. Disturbances with standard deviations of 0.1 °C/s for the temperatures and 0.001 Pa/s for the pressure are added to the right hand side of the corresponding equations for the nonlinear system before integrating every time step (process noise).

Fig. 9 shows the results for the simulations including noise and disturbances, where the gray thin lines show the sensor readings used by the LQG feedback controller. Even with large amounts of disturbances and noise, the system is stabilized around the desired operation point and the estimated state variables agree with the true behavior of the nonlinear system. Although the stabilization of air outflow temperature is a task that can be easily handled by a model-free control strategy, such as a proportional–integral (PI) controller, the proposed model-based architecture allows for the real-time estimation of the solid matrix temperatures and of the radiation flux.

4.3. Cloud passing with LQG

To formulate the control problem, again the system is extended to consider the pressure drop as a state using Eq. (14). However, because during this scenario the radiation flux variations are fast, its dynamics cannot be represented by Eq. (15), and instead $G(t)$ is considered as an exogenous input to the system. As a consequence the following analysis rests on the assumption that the controller has access to the time series of the incoming radiation flux. In practice this can be achieved using cloud coverage prediction techniques that have been demonstrated in several studies (Augsburger and Favrat, 2013; García et al., 2018; Lopes et al., 2019) The nonlinear system, described by Eqs. (3) and (14), is simulated using LQG control based on the linearization of the extended system. The simulation considers the time-dependent radiation flux shown in Fig. 6*a*) as an external disturbance and measurements from air temperature and pressure sensors located at the receiver outlet. For this scenario, the system is linearized around the equilibrium point

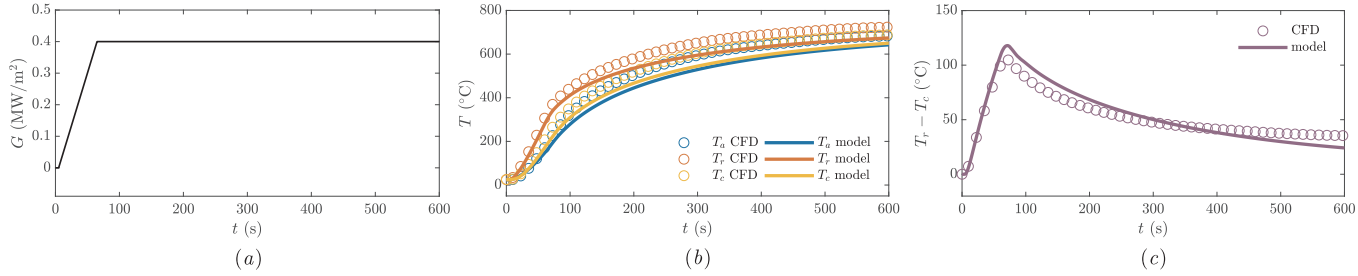

Fig. 7. (*a*) Time-dependent radiation flux used for the cold start-up scenario. CFD and model results during a cold start-up procedure: (*b*) air outflow temperature and solid matrix temperatures in the front and rear sections of the receiver, and (*c*) temperature differences within the absorber.

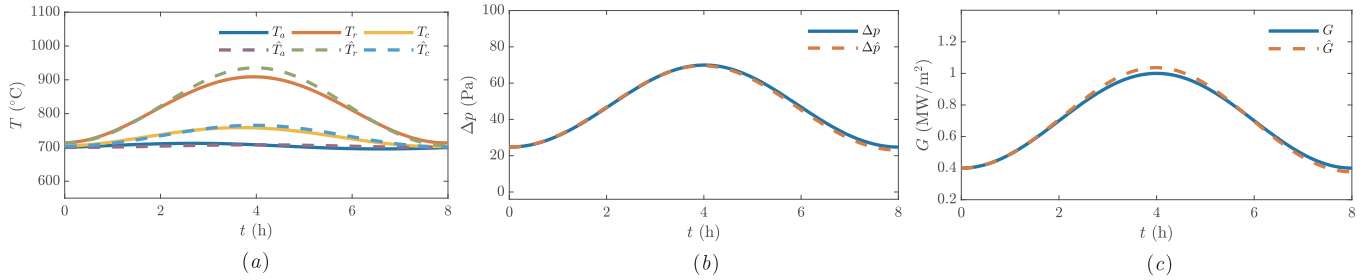

Fig. 8. True and estimated state variables as a function of time during clear-sky daily operation using LQG control. (*a*) Air outflow temperature and solid matrix temperatures in the front and rear sections of the receiver. (*b*) Pressure drop. (*c*) Radiation flux.

$T_a = 700$ °C, $T_r = 904.3$ °C, $T_c = 751$ °C, $\Delta p = 70.13$ Pa, $G = 1$ MW/m^2, and $u = 0$ Pa/s.

Results for the simulation with LQG control are shown in Fig. 10, where the dashed curves correspond to the estimates of the state variables and the solid curves correspond to the actual behavior of the state variables of the nonlinear system. As for the previous scenario, the controller stabilizes the air outflow temperature, only this time information of the radiation flux is required due to the fast transients. However, the controlled system still exhibits important temperature changes in the front section of the absorber, as shown in Fig. 10*a*). Nevertheless, the size of these fluctuations decreases to less than half of that observed for the uncontrolled case in Fig. 6*b*). Moreover, these variations can be monitored via state estimation, which may be useful to get statistics of the temperature cycling of the solid matrix for thermal fatigue studies.

As in the previous section, zero-mean Gaussian noise and disturbances with specified standard deviations are included in the simulations to assess the robustness of the LQG controller. Measurement noise with a standard deviation of 20 °C and 4 Pa is added directly to the air outflow temperature and pressure sensor readings, respectively. Disturbances with standard deviations of 0.1 °C/s for the temperatures and 0.001 Pa/s for the pressure are added to the right hand side of the corresponding equations for the nonlinear system before integrating every time step (process noise).

Fig. 11 shows the results for the simulations including noise and disturbances, where the gray thin lines show the sensor readings used by the LQG feedback controller. Even with large amounts of disturbances and noise, the system is stabilized around the desired operation point and the estimated state variables agree with the true behavior of the nonlinear system.

The effect of tuning the LQR cost function on the response of the closed-loop system during the passing of a cloud is explored. The air outflow temperature, pressure drop and blower control input are computed for different values of the actuation cost between $\mathbf{R} = 0.1$–1000, as shown in Fig. 12. Tuning the LQR controller results in a trade-off between a cheaper actuation expenditure and a more effective controller.

4.4. Cold start-up with LQG

The cold start-up procedure involves actuation of the heliostat field and blower to modify the radiation flux and the suction pressure, respectively. Therefore, to formulate the control problem for this scenario, the pressure drop Δp, the radiation flux G, and the radiation flux rate of change $\dot{G}$ are considered as state variables. Their time evolution is modeled by Eq. (14) and the following differential equation

$$\ddot{G} = -\dot{G} + v, \tag{16}$$

which is to be interpreted as an equation of motion, where G and $\dot{G}$ are directly related to the position and velocity of the heliostats and v represents an actuation force that is the second input to the system along with u. The coefficients of the terms in Eq. (16) that represent the effects of inertia and friction are set to one for the sake of simplicity, but these values should be modified accordingly for the application to a real system. The extended nonlinear system, described by Eqs. (3), (14) and (16), is simulated using LQG control based on the linearization of the extended system. The simulation starts from rest, it considers the same target state as in the exercise presented in Section 4.1.3, and feedback is obtained from measurements of the radiation flux (position of the heliostats) and of the temperature and pressure of the air at the outlet of the receiver. For this scenario, the system is linearized around the equilibrium point $T_a = 700$ °C, $T_r = 713.7$ °C, $T_c = 703.5$ °C, $\Delta p = 24.76$ Pa, $G = 0.4$ MW/m^2, $\dot{G} = 0$ MW/(s m^2), $u = 0$ Pa/s, and $v = 0$ MW/(s^2 m^2).

Results for the simulation with LQG control are shown in Fig. 13, where the dashed curves correspond to the estimates of the state variables and the solid curves correspond to the actual behavior of the state variables of the nonlinear system. Compared to the linear ramp-up control strategy shown in Fig. 7, the LQG controller is able to drive the system to the desired operating condition much faster and at the same time reduce the transient temperature differences within the solid matrix. This is achieved by delaying the blower actuation to speed up the heating of the ceramic absorber.

As in the two previous scenarios, zero-mean Gaussian noise and disturbances with specified standard deviations are included in the simulations to assess the robustness of the LQG controller. Measurement noise with a standard deviation of 20 °C, 4 Pa and 40 kW/m^2 is added

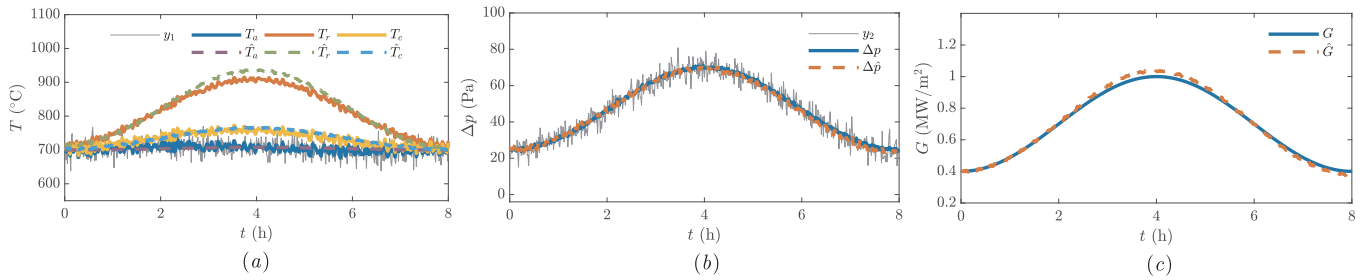

Fig. 9. True, measured and estimated state variables as a function of time during clear-sky daily operation using LQG control. (*a*) Air outflow temperature and solid matrix temperatures in the front and rear sections of the receiver. (*b*) Pressure drop. (*c*) Radiation flux.

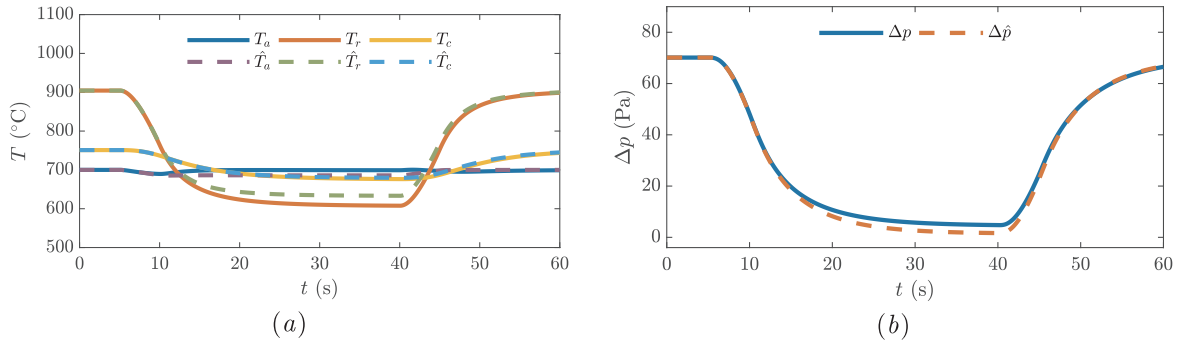

Fig. 10. True and estimated state variables as a function of time during the passing of a cloud using LQG control. (*a*) Air outflow temperature and solid matrix temperatures in the front and rear sections of the receiver. (*b*) Pressure drop.

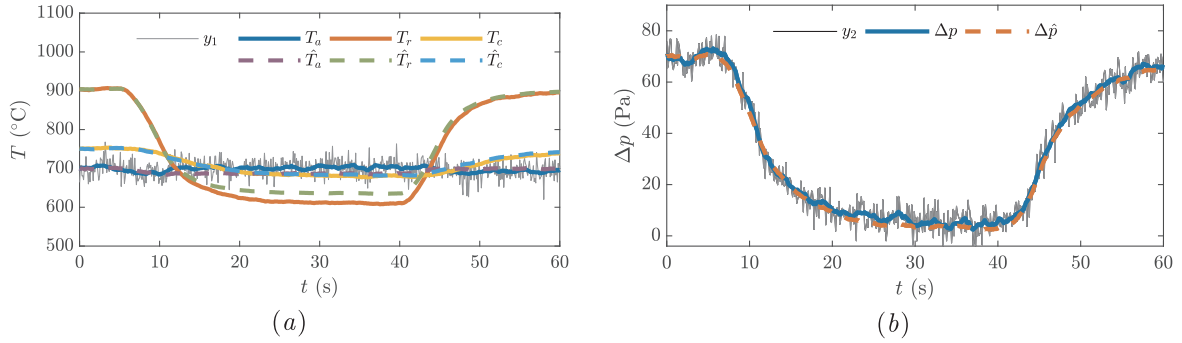

Fig. 11. True, measured and estimated state variables as a function of time during the passing of a cloud using LQG control. (*a*) Air outflow temperature and solid matrix temperatures in the front and rear sections of the receiver. (*b*) Pressure drop.

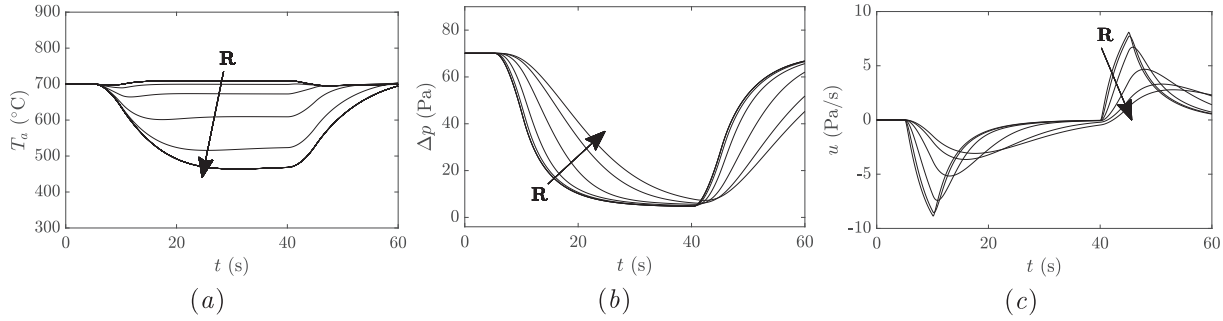

Fig. 12. Feedback control during the passing of a cloud for different actuation costs between $\mathbf{R}$ = 0.1–1000. (*a*) Air outflow temperature. (*b*) Pressure drop. (*c*) Control input.

directly to the air outflow temperature, pressure, and radiation flux sensor readings, respectively. Disturbances with standard deviations of 0.1 °C/s for the temperatures and 0.001 Pa/s for the pressure are added to the right hand side of the corresponding equations for the nonlinear system before integrating every time step (process noise).

Fig. 14 shows the results for the simulations including noise and disturbances, where the gray thin lines show the sensor readings used by the LQG feedback controller. Again, the controller is able to reject disturbances noise and attenuate large amounts of noise while the estimated state variables agree with the true behavior of the nonlinear system.

The effect of tuning the LQR cost function on the response of the closed-loop system in the cold start-up scenario is explored. The air outflow temperature, pressure drop, temperature differences within the solid matrix, and the radiation flux hitting the receiver are computed for different values of the state deviation cost for $\dot{G}$, representing the velocity of the heliostats, between $\mathbf{Q}_{55}$ = 0.005–5, as shown in Fig. 15. Increasing the value of $\mathbf{Q}_{55}$ translates into a more aggressive heliostat actuation, that results in a faster thermal response at the expense of a higher overshoot in the temperature differences within the absorber. Being able to tune the controller is key to get a quick start-up of the receiver while avoiding thermal shock of the ceramic materials for a given receiver design.

5. Conclusions

We propose a data assimilation framework to perform simultaneous feedback control and state estimation in a volumetric solar receiver module using a physics-based model and sensors located in the outflow stream of air. First, we formulated a model for the conjugate heat transfer problem using only three degrees of freedom, thus making online calculations viable. Results are then compared to those obtained from full three-dimensional CFD and we show that our model is able to capture the relevant dynamics.

The proposed framework was tested for three simulated transient scenarios to verify how some common issues in VSRs can be addressed. Firstly, during clear-sky daily operation, blower actuation is used to stabilize the outflow temperature and at the same time get an estimate

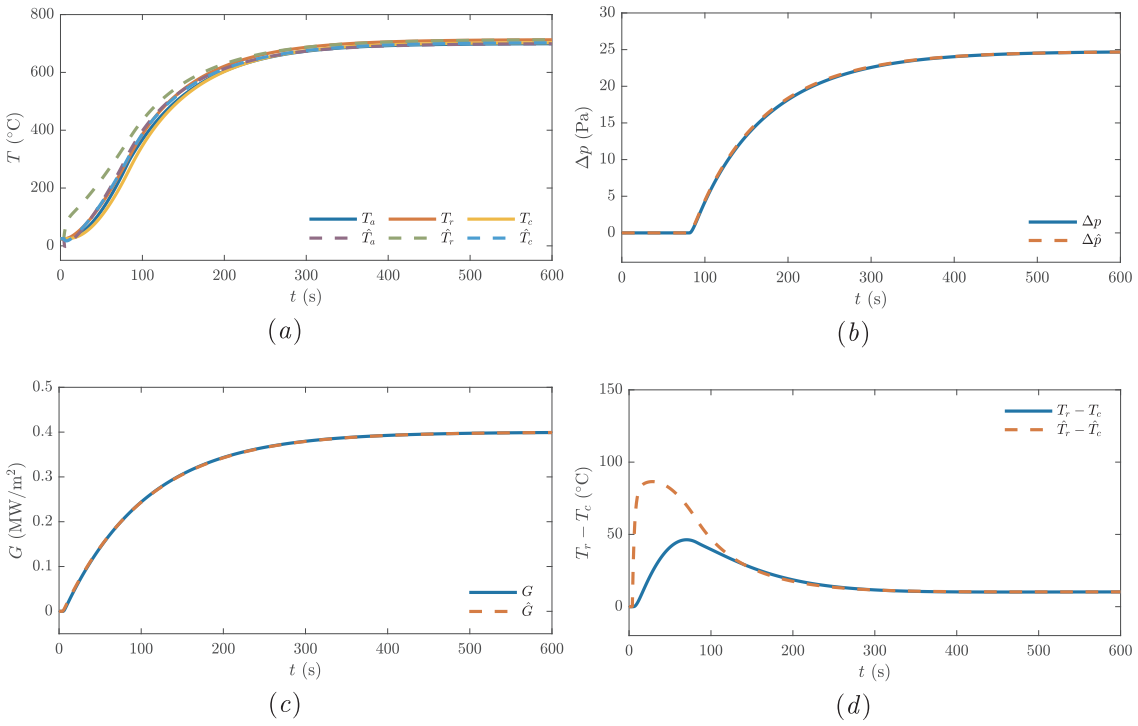

Fig. 13. True and estimated state variables as a function of time during a cold start-up procedure using LQG control. (*a*) Air outflow temperature and solid matrix temperatures in the front and rear sections of the receiver. (*b*) Pressure drop. (*c*) Radiation flux. (*d*) Temperature difference within the absorber.

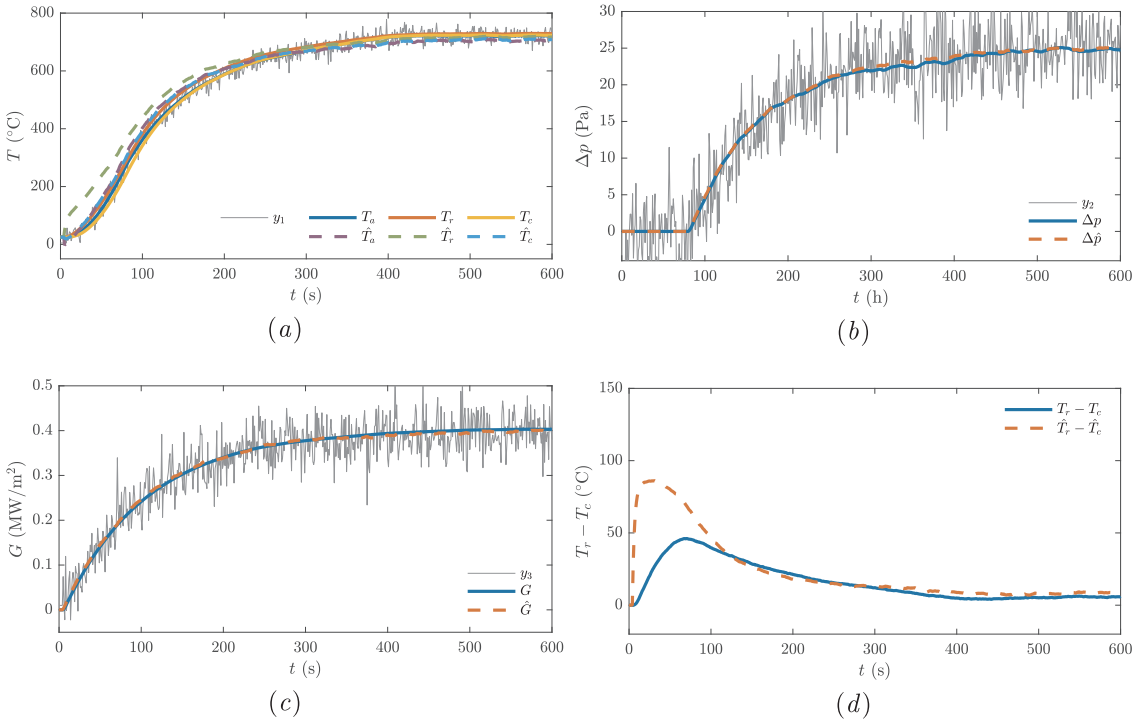

Fig. 14. True, measured and estimated state variables as a function of time during a cold start-up procedure using LQG control. (*a*) Air outflow temperature and solid matrix temperatures in the front and rear sections of the receiver. (*b*) Pressure drop. (*c*) Radiation flux. (*d*) Temperature difference within the absorber.

of the temperature cycling in the solid matrix and of the radiation flux hitting the absorber, which may be used to compute the thermal efficiency of the receiver and assess its state of health in real time. Secondly, during the passing of a cloud, the fluid temperature at the outlet is stabilized using blower actuation and assuming that information of the radiation flux drop is available, adding to the reliability of the downstream processes. Thirdly, for a cold start-up procedure, the system is guided from rest to steady state operation by actuating both, the suction pressure and the amount of radiation flux hitting the receiver. The controller may be tuned to trade between a faster start-up, increasing the energy yield, or a smaller overshoot of the temperature differences within the solid matrix, decreasing the risk of thermal shock. Artificial noise and disturbances are added to the system for all scenarios and the LQG controller proves to be robust, rejecting

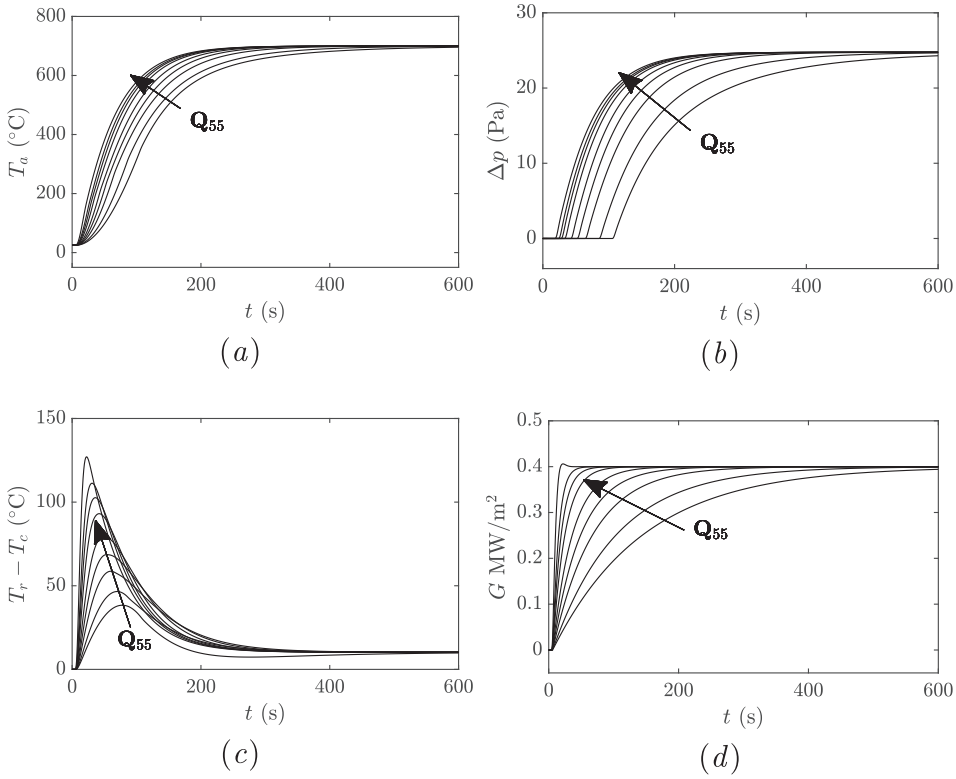

Fig. 15. Feedback control during a cold start-up procedure for different deviation costs for heliostat velocity between $\mathbf{Q}_{55}$ = 0.005–5. (*a*) Air outflow temperature. (*b*) Pressure drop. (*c*) Temperature differences within the absorber. (*d*) Radiation flux.

disturbances and attenuating noise, as well as compensating for model uncertainty.

Interesting directions for future work consider the extension of the heat transfer model to account for transport processes between absorber modules, including the effect of temperature, radiation flux and mass flow rate distributions in the transverse plane. In addition, we are planning to test the feedback control and state estimation in an experimental setup, considering its interaction with the aiming control of the heliostat field. Online indirect measurements of the temperatures inside the ceramic absorber opens up new avenues for applied research, such as thermal fatigue and thermal shock studies using real operation data. Still, much progress is needed in these areas for the volumetric solar receiver to become a mature technology.

Declaration of Competing Interest

None.

Acknowledgements

This work has been supported by Enerbosch SpA and by CORFO Chile under the grant CORFO-Contratos Tecnológicos 18COTE-89602.

References

Abuseada, M., Ozalp, N., Ophoff, C., 2019. Numerical and experimental investigation of heat transfer in a solar receiver with a variable aperture. Int. J. Heat Mass Transf. 128, 125–135.
Ansys Inc., 2011. Ansys CFX-Solver modeling guide. Release 14.0.
Ansys Inc., 2012. Introduction to Ansys meshing. Release 14.5.
Aström, K.J., Murray, R.M., 2010. Feedback Systems: An Introduction for Scientists and Engineers. Princeton University Press.
Atif, M., Al-Sulaiman, F.A., 2017. Energy and exergy analyses of solar tower power plant driven supercritical carbon dioxide recompression cycles for six different locations. Renew. Sustain. Energy Rev. 68 (2016), 153–167.
Augsburger, G., Favrat, D., 2013. Modelling of the receiver transient flux distribution due to cloud passages on a solar tower thermal power plant. Sol. Energy 87 (1), 42–52.
Ávila-Marín, A.L., 2011. Volumetric receivers in solar thermal power plants with central receiver system technology: a review. Sol. Energy 85 (5), 891–910.
Becker, M., Fend, T., Hoffschmidt, B., Pitz-Paal, R., Reutter, O., Stamatov, V., Steven, M., Trimis, D., 2006. Theoretical and numerical investigation of flow stability in porous materials applied as volumetric solar receivers. Sol. Energy 80, 1241–1248.
Cagnoli, M., Savoldi, L., Zanino, R., Zaversky, F., 2017. Coupled optical and CFD parametric analysis of an open volumetric air receiver of honeycomb type for central tower CSP plants. Sol. Energy 155, 523–536.
Cengel, Y.A., Ghajar, A.J., 2011. Heat and mass transfer: a practical approach. McGraw Hill, 671:52.
Conn, A.R., Gould, N.I., Toint, P.L., 2000. Trust region methods. SIAM.
Crespi, F., Toscani, A., Zani, P., Sánchez, D., Manzolini, G., 2018. Effect of passing clouds on the dynamic performance of a CSP tower receiver with molten salt heat storage. Appl. Energy 229 (January), 224–235.
Gielen, D., 2012. Renewable energy technologies: cost analysis series. Concentrat. Sol. Power. IRENA 1 (2), 1–48.
Doyle, J.C., Francis, B.A., Tannenbaum, A.R., 2013. Feedback Control Theory. Courier Corporation.
Fend, T., Schwarzbözl, P., Smirnova, O., Schöllgen, D., Jakob, C., 2013. Numerical investigation of flow and heat transfer in a volumetric solar receiver. Renew. Energy 60, 655–661.
García, J., Soo Too, Y.C., Padilla, R.V., Beath, A., Kim, J.S., Sanjuan, M.E., 2018. Dynamic performance of an aiming control methodology for solar central receivers due to cloud disturbances. Renew. Energy 121, 355–367.
Gómez, M.A., Patiño, D., Comesa na, R., Porteiro, J., Álvarez Feijoo, M.A., Míguez, J.L., 2013. CFD simulation of a solar radiation absorber. Int. J. Heat Mass Transf. 57 (1), 231–240.
IEA, 2010. Technology Roadmap: Concentrating Solar Power. Technical report, International Energy Agency, Paris, France.
Kandlikar, S., Garimella, S., Li, D., Colin, S., King, M.R., 2005. Heat transfer and fluid flow in minichannels and microchannels. Elsevier.
Kaviany, M., 2012. Principles of Heat Transfer in Porous Media. Springer Science & Business Media.
Kribus, A., Ries, H., Spirkl, W., 1996. Inherent limitations of volumetric solar receivers. J. Sol.Energy Eng. 118 (3), 151–155.
Li, Q., Bai, F., Yang, B., Wang, Z., El Hefni, B., Liu, S., Kubo, S., Kiriki, H., Han, M., 2016. Dynamic simulation and experimental validation of an open air receiver and a thermal energy storage system for solar thermal power plant. Appl. Energy 178, 281–293.
Lopes, F.M., Conceicao, R., Silva, H.G., Fasquelle, T., Salgado, R., Canhoto, P., Collares-Pereira, M., 2019. Short-term forecasts of DNI from an integrated forecasting system (ECMWF) for optimized operational strategies of a central receiver system. Energies 12 (7).
Lott, M.C., Kim, S.-I., 2014. Technology Roadmap: Energy Storage. Technical report, International Energy Agency, International Energy Agency. Paris, France.

Mehos, M., Turchi, C., Vidal, J., Wagner, M., Ma, Z., Ho, C., Kolb, W., Andraka, C., Mehos, M., Turchi, C., Vidal, J., Wagner, M., Ma, Z., Ho, C., Kolb, W., Andraka, C., Kruizenga, A., NREL, 2017. Concentrating solar power: Gen3 demonstration roadmap. Technical Report January, National Renewable Energy Laboratory - NREL, Golden, Colorado. NREL/TP-5500-67464.

Modest, M.F., 2013. Radiative Heat Transfer. Academic press.

REN21 Secretariat, 2012. REN21. Renewables 2012-Global Status Report. REN21, Paris, France.

REN21 Secretariat, 2018. REN21. Renewables 2018-Global Status Report. REN21, Paris, France.

Reyes-Belmonte, M.A., Sebastián, A., Romero, M., González-Aguilar, J., 2016. Optimization of a recompression supercritical carbon dioxide cycle for an innovative central receiver solar power plant. Energy 112, 17–27.

Samanes, J., Garcia-Barberena, J., 2014. A model for the transient performance simulation of solar cavity receivers. Sol. Energy 110, 789–806.

Shampine, L.F., Reichelt, M.W., 1997. The MATLAB ODE Suite. SIAM J. Scient. Comput. 18, 1–22.

Stadler, H., Maldonado, D., Offergeld, M., Schwarzbözl, P., Trautner, J., 2019. CFD model for the performance estimation of open volumetric receivers and comparison with experimental data. Sol. Energy 177 (December 2018), 634–641.

Stengel, R.F., 1994. Optimal Control and Estimation. Courier Corporation.

Tehrani, S.S.M., Taylor, R.A., 2016. Off-design simulation and performance of molten salt cavity receivers in solar tower plants under realistic operational modes and control strategies. Appl. Energy 179, 698–715.

Worth, D.J., Spence, A., Crumpton, P.I., Kolaczkowski, S.T., 1996. Radiative exchange between square parallel channels in a concentric monolith structure. Int. J. Heat Mass Transf. 39, 1463–1474.